Journal of the Iranian Chemical Society (2019) 16:1291–1300
https://doi.org/10.1007/s13738-019-01606-5

ORIGINAL PAPER

Design of CuO/SnO_2 heterojunction photocatalyst with enhanced UV light-driven photocatalytic activity on congo-red and malachite green dyes

D. Selleswari[1] · P. Meena[2] · D. Mangalaraj[3]

Received: 20 October 2018 / Accepted: 19 January 2019 / Published online: 24 January 2019

Abstract
In this work, $CuO–SnO_2$ composite thin films were prepared by spray pyrolysis method using copper acetate and tin chloride dihydrate as raw materials. The structural, morphological and optical properties of the prepared nanocomposite were systematically investigated by X-ray diffraction (XRD), Scanning electron microscope (SEM) and UV–Vis absorption spectra analysis. The calculated grain size was in the range from 27 to 54 nm. SEM images reveal a spherical shaped morphology with an average diameter of around 10–15 nm. EDX analysis confirms the composition of the deposited thin films. The band gap of the composite thin films obtained from the optical absorption spectra is observed to be in the range from 2.98 to 3.67 eV. The photocatalytic activity of the nanocomposite was investigated using congo-red (CR) and malachite green (MG) under UV light irradiation. The results showed that the $CuO–SnO_2$ composite exhibits superior photocatalytic performance towards CR such as high degradation efficiency (97%) and long term stability (only 3% loss) after a seven cycles test. This enhanced photocatalytic activity can be attributed to the low recombination probability of photo-induced carriers due to the efficient charge transfer in the nanocomposites. The improved photocatalytic mechanism of $CuO–SnO_2$ composite is also discussed in brief.

Keywords $CuO–SnO_2$ composite · Spray pyrolysis · UV light · Photocatalyst · Congo-red

Introduction

In recent years, environmental pollution has become one of the major issues in developing and developed countries around the world. As a result, continuous efforts have been tailored to enhance innovative technologies to remediate the polluted environment. It is well known that photocatalysis is an attractive tool due to its high efficiency and relatively low cost [1]. Numerous techniques have been developed for the removal of pollutants from wastewaters to limit their impact on the environment. Photocatalytic treatment is one of the most effective techniques for the degradation of dye pollutants in waste water [2–4]. Recently, metal oxide semiconductors like ZnO, TiO_2, SnO_2, CuO, NiO, WO_3, and Fe_3O_4 have been proved to be potential candidates for many applications such as solar cells, gas sensors, bio sensors, photocatalysts, electrochemical cells, field emitters and optoelectronic devices [5]. There are many reports on the photocatalytic degradation of organic compounds using metal oxide semiconductors as photocatalysts [6–11]. Among the different types of metal oxides, tin dioxide (SnO_2) is a stable and largely n-type semiconductor material with a band gap (E_g) around 3.7 eV. It finds wide uses in various applications such as gas sensors, photosensors, antistatic coatings, photocatalysts and so on [12]. CuO is an important p-type semiconductor with a band gap of 1.2 eV. The photocatalytic and electrochemical properties of SnO_2/CuO nanocomposites synthesized by different techniques have been reported by earlier researchers [9–11]. Among the various techniques, the chemical spray pyrolysis method (CPS) is a simple and cost effective method for the deposition of large area thin films. This method enables deposition of the thin films with

✉ P. Meena
drpmeena@gmail.com

[1] PG and Research Department of Physics, Chikkaiah Naicker College, Erode 638004, India

[2] Department of Physics, P.S.G.R. Krishnammal College for Women, Coimbatore 641004, India

[3] Department of Nanoscience and Nanotechnology, Bharathiar University, Coimbatore 641046, India

controllable composition and microstructure at moderate temperatures (100–500 °C). This method also has the advantage that it does not require high quality targets or vacuum.

Xia et al. [13] have reported the Photocatalytic degradation of Acid Blue 62 using CuO–SnO_2 nanocomposite photocatalyst under simulated sunlight. It was observed that the CuO–SnO_2 nanocomposite showed much higher photocatalytic activity in the treatment of dyes in wastewater under simulated sunlight irradiation when compared to Degussa P25 TiO_2. Kumar et al. [14] have synthesized SnO_2/CuO nanocomposite using combustion synthesis and investigated the photo degradation properties of malachite green dye under UV light irradiation. In an attempt to further improve its photocatalytic performance, in the present work, SnO_2/CuO nanocomposite has been prepared by the spray pyrolysis technique and its effectiveness in the photocatalytic degradation of CR and MR dyes under UV light irradiation studied. To the best of the author's knowledge, this is the first preliminary report about structural, optical and photocatalytic properties of SnO_2/CuO nanocomposite prepared by the simple spray pyrolysis method.

Experimental procedure

Materials

High purity copper acetate and tin chloride were purchased from Sigma-Aldrich (purity 99.97%). NH_4OH, congo-red and malachite green dyes were purchased from Merck. All the chemical reagents were used without further purification. Distilled water was used throughout the experiment.

Synthesis of CuO/SnO_2 composite thin films

Pure CuO, SnO_2 and its composites were prepared by spray pyrolysis technique. Appropriate amount of precursor materials (copper acetate, and tin chloride) were dissolved in a solution of deionized water and ethanol. A few drops of HCl were added to make the solution clear. The ratio of CuO:SnO_2 is varied (0, 0.5, 1 and 1.5 mol%). The spraying process was done using a laboratory designed glass atomizer with an output nozzle of about 1 mm. The films were deposited on preheated glass substrates at a temperature of 500 °C, under optimized conditions. The spray time was 10 s and a constant spray interval of 3 min was maintained. The carries gas was maintained at a pressure of 10^5 N m^{-2}, the distance between the nozzle and substrate was about 29 cm and the solution flow rate was 5 ml/min. To explore the influence of film thickness on the parameters under investigation, the films were prepared with different thickness in the range of 400, 450 and 500 nm.

Characterization techniques

The phase purity of the synthesized films was analyzed by X-ray diffraction (XRD-Bruker-AXS D8 Advance, Cu Kα radiation). The elemental compositions of the samples were examined by studying the energy dispersive spectra (EDS, obtained by employing JEOL Model JED-2300). The microstructure was analyzed using scanning electron microscope (JEOL Model JSM-6390LV). The UV–Vis spectrum was obtained using a Perkin Elmer UV/VIS/NIR Lambda 19 spectrophotometer. Photoluminescence spectra of the samples were obtained at room temperature using Cary Eclipse (el02045776) Fluorescence spectrophotometer with He–Cd laser (excitation wavelength of 350 nm) as the exciting source. Air wedge method was used to determine the thicknesses of the obtained samples.

Photocatalytic activity set up

Rajamanickam et al. [15] have given a detailed description of the photocatalytic set up. A 500 W Xenon lamb is used as the UV light source to trigger the photocatalytic reaction. The photocatalytic reactor consists of a specially designed quartz glass cylinder (30 cm width and 40 cm height). For the photocatalytic process, two 25 mm × 75 mm glass plates coated with the films were immersed in 25 ml each of the dye solutions (CR and MG of 15 mg/l concentration) kept in cylindrical glass reactors. The coated glass/dye solution was irradiated in the horizontal direction and the distance between the UV lamp and the glass/dye solution was kept within 25 cm. The UV–Vis–NIR measurement was performed using PerkinElmer lambda 25 spectrophotometer to determine the absorption. The degradation of the CR and MG dyes was studied using the ratio of initial (C_0) to final (C) concentration.

Results and discussion

X-ray diffraction (XRD) analysis

The crystallinity, phase, and purity of the samples were determined by X-ray diffraction (XRD). The XRD patterns for the CuO–SnO_2 composite thin films with different ratios of CuO and SnO_2 are shown in Fig. 1. All the diffraction peaks of pure CuO and SnO_2 can be indexed to monoclinic and tetragonal structures respectively. The results are good accordance with the standard JCPDS data (45-0937 and 45-1445). The XRD pattern of CuO/SnO_2 composites shows the mixed phase of CuO and SnO_2 (77-0447). The XRD patterns are found to be identical for all ratios and the CuO

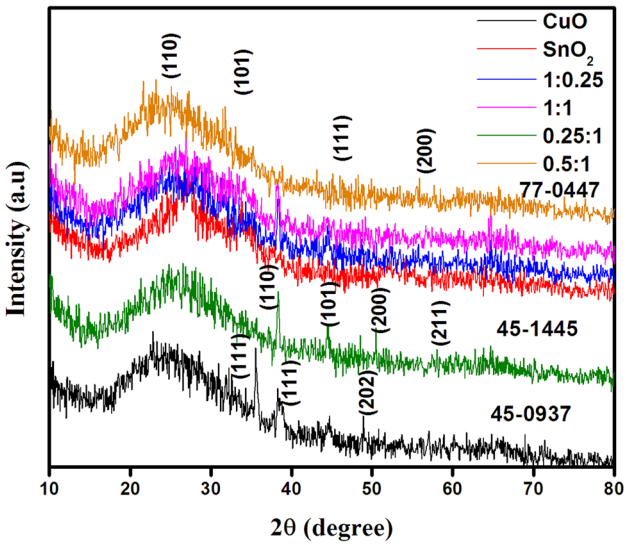

Fig. 1 XRD pattern of the CuO, SnO_2 and its different ratio

Table 1 Shows the average grain sizes, thickness and band gap of the films

Sample	Thickness (nm)	Grain size (nm)
CuO	508	44
SnO_2	470	35
1:0.5	492	40
1:75	495	43
0.5:1	485	41
1:1	520	54

molecules are well integrated into the SnO_2 lattice. No additional peaks are observed, indicating that there is no change in the crystalline structure of the CuO–SnO_2 composite thin films due to the different ratios. However, the intensity of the main peaks is found to decrease as the ratio changed, which suggests that the changing ratio may manipulate the crystalline state at which CuO–SnO_2 changes from amorphous to crystalline state. The average crystallite size can be determined through full-width at half maximum (FWHM) of X-ray diffraction peak using the Debye–Scherer's equation [16]. The grain size calculated from different peaks is found to range from 27 to 54 nm confirming the nanostructure of the prepared thin films (Table 1).

Scanning electron microscope analysis

Figure 2a–f shows the SEM pictures of all the films. The SEM images of pure CuO and SnO_2 (Fig. 2a, b, respectively) exhibit a spherical shaped morphology with the average diameter of particles around 35–45 nm. The formation of spherical particles indicates the effectiveness of annealing in the removal of the organic compounds used in the synthesis. A brittle glass like morphology is exhibited by the SEM images of CuO–SnO_2 composite thin films (Fig. 2c–f). It is observed that the morphology varies with the ratios of the constituents. The elemental composition of the films was analyzed using EDS and the corresponding profile is shown in Fig. 3a–f. Pure CuO and SnO_2 films indicate the existence of only Cu, O and Sn, O elements, respectively, while the entire composite films exhibit the presence of Cu, Sn and O elements. These results ensure the formation of CuO/SnO_2 composite films. The presence of Si element in the composition is attributed to the grid used in EDS measurements. The calculated stoichiometry ratio from the EDS measurements is found to be in good agreement with the precursors used for preparation.

UV–Vis absorption spectra analysis

The optical property and band gap of the films were studied by analysing the UV–Vis absorption spectra. Figure 4a shows the UV–Visible absorption spectra of the films. In pure SnO_2, the sharp absorption observed around 300–350 nm corresponds to the band gap of SnO_2 (3.6 eV). A considerable red shift in the absorption edge and a decrease in the band gap of the films were observed for the CuO/SnO_2 films. The slight decrease in the band gap of the film observed after integration of the CuO into SnO_2 is attributed to the lower band gap of CuO. To further confirm the band gap, the Tauc plot is used and the absorbance coefficient (α) was calculated from the raw absorbance data to obtain the optical band gap (E_g). The band gap values were determined by the extrapolation of the linear portion of the $(\alpha h\nu)^2$ versus photon energy ($h\nu$) curve [17]. The optical band gap energy values were found to be 3.36 eV and 1.6 eV for pure SnO_2 and CuO respectively. Impressively, the band gap decreases to 3.0 eV for CuO/SnO_2 (1:1) film.

Photoluminescence spectra analysis

Figure 5 shows the room temperature PL spectra of the films. For the pure SnO_2 sample, emission peaks are observed at 367 nm and 495 nm, which correspond to UV emission and green emission, respectively. The UV emission is due to the near band edge emission (NBE) from the holes in the valence band and the radiative recombination of electrons in the conduction band [18]. The green emission is attributed to the electron transition facilitated through defect levels in the band gap and oxygen vacancies produced during the annealing process [19]. In CuO, the emission peaks at 530 nm and 590 nm are attributed to the band edge emission and oxygen vacancies respectively [20]. The spectrum of SnO_2/CuO nanocomposite (1:1 ratio) shows only a broad band with a

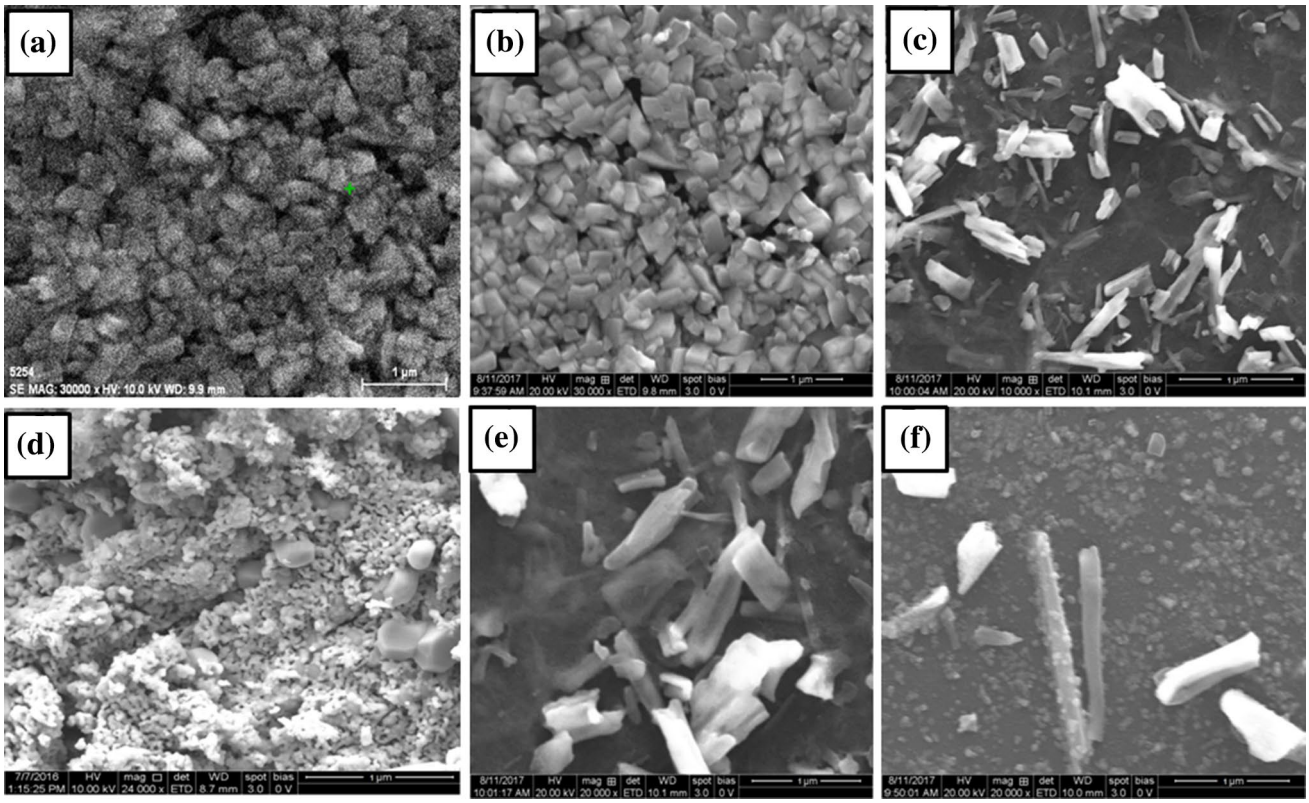

Fig. 2 SEM images of **a** CuO, **b** SnO_2, **c** 1:1, **d** 1:0.25, **e** 1:0.5, **f** 0.25:1 and **g** 0.5:1

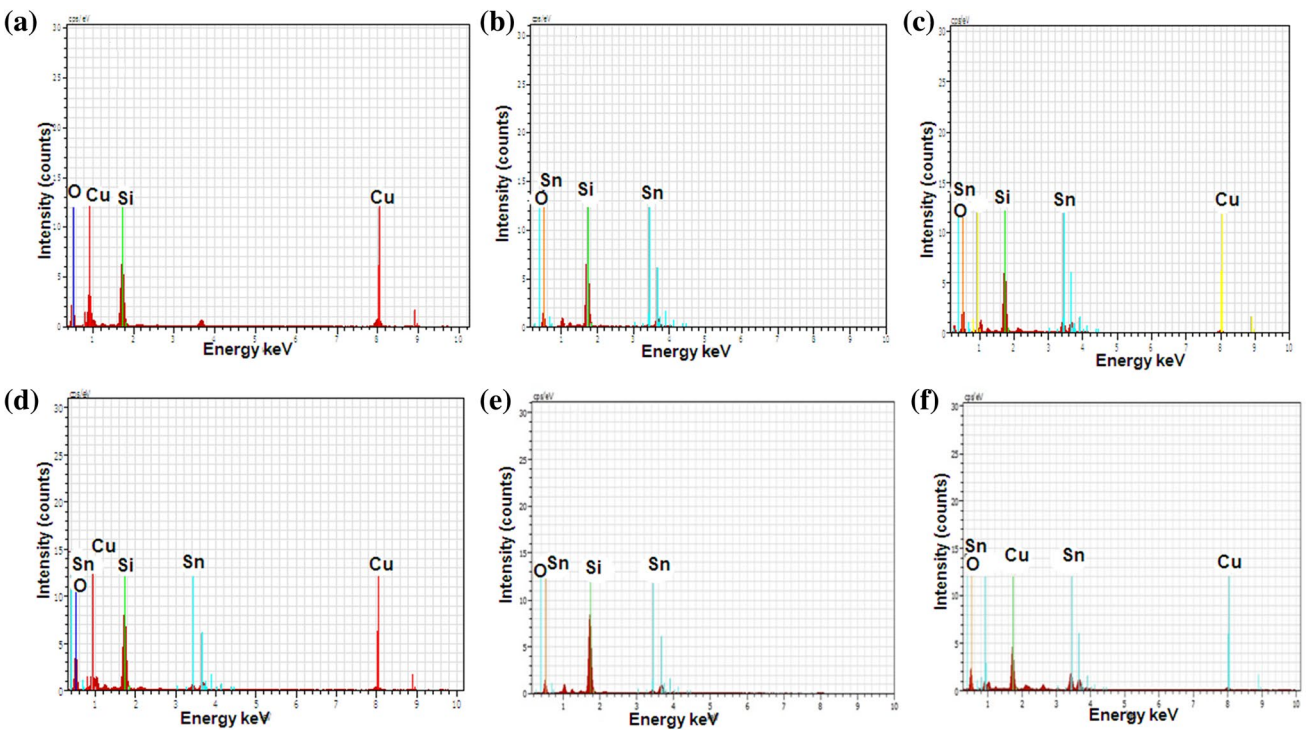

Fig. 3 EDS images of **a** CuO, **b** SnO_2, **c** 1:1, **d** 1:0.25, **e** 1:0.5, **f** 0.25:1 and **g** 0.5:1

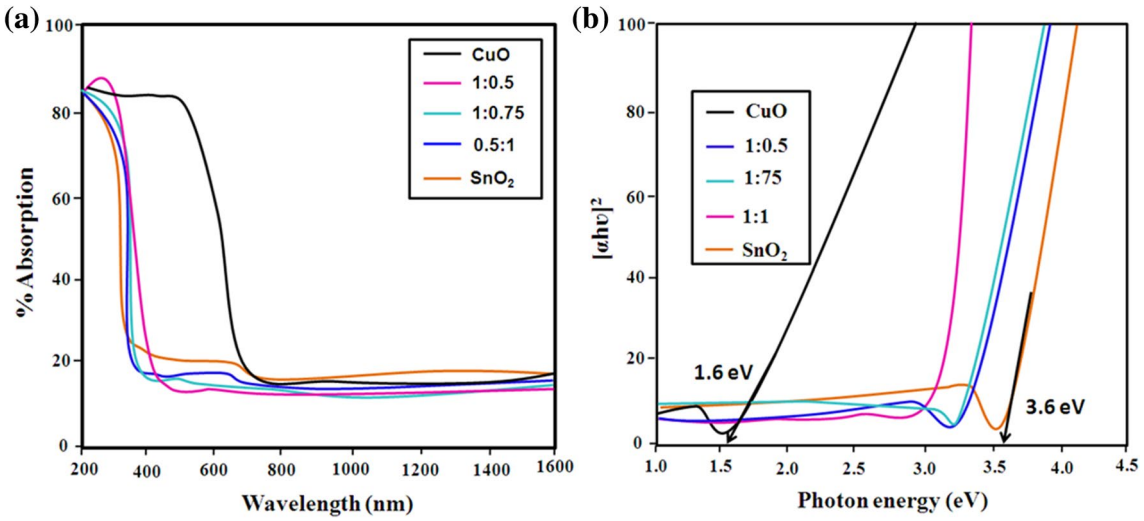

Fig. 4 UV–Vis spectra of the films **a** absorption spectra and **b** band gap energy plot

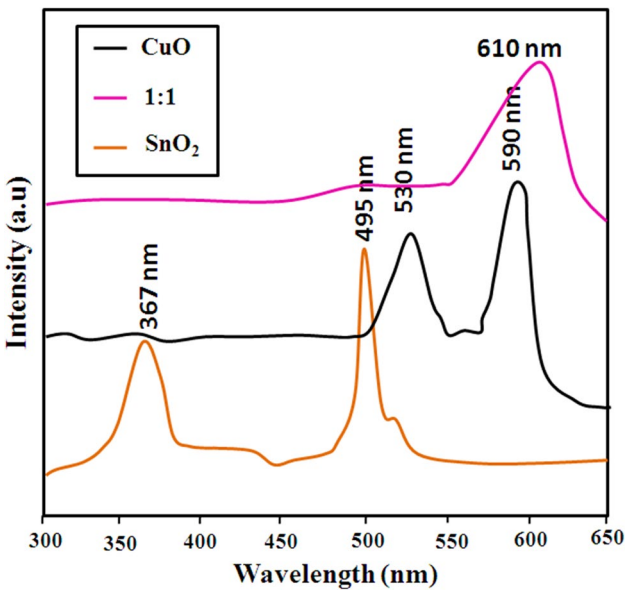

Fig. 5 Room temperature photoluminescence spectra of the films

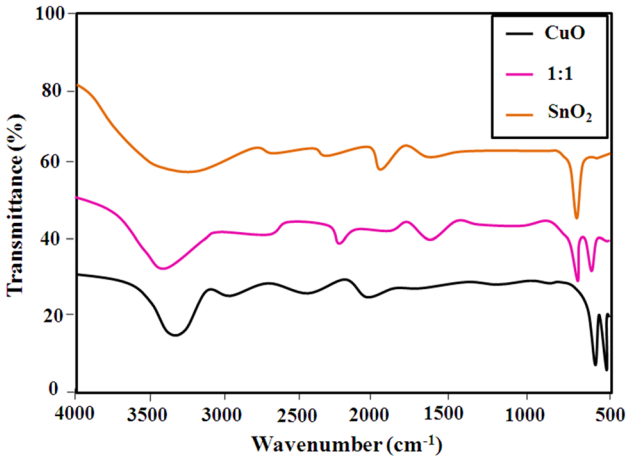

Fig. 6 FTIR spectra of the films

strong orange emission centered at around 610 nm. This is attributed to the interaction between oxygen vacancies and the interfacial tin vacancies [21].

FTIR analysis

The functional groups the films were analyzed using FTIR spectra and the results are shown in Fig. 6. The strong vibration band observed around 615 cm^{-1}, can be attributed to the ν (Sn–O–Sn) of the tin oxide framework [22]. In pure CuO (there are two noticeable absorption peaks around 562 and 525 cm^{-1}), which can be attributed to the vibrations of the Cu–O bonds [23]. The broad absorption band at 3425.12 cm^{-1} observed in all the films, arises due to the stretching mode of O–H group and reveals the existence of the small amount of water absorbed by the CuO nanostructure [24]. In CuO/SnO_2 nanocomposite (1:1), the vibrational band (at 590 cm^{-1}) can be assigned as a metal–oxygen (Sn–O and Cu–O) stretching vibration [25], which confirms the configuration of the doped SnO_2/CuO and CuO/SnO_2 nanocomposites.

Photocatalytic studies

Absorbance and degradation test

In the present study, CR and MG dyes have been used as the model organic dyes to study the photocatalytic activity of the deposited films under UV light illumination.

The characteristic peaks around 500 nm and 610 nm were selected as the reference peaks for the CR and MG dyes respectively. Figure 7 shows the UV absorption graph of the catalyst for the CR dye and Fig. 8 for the MG dye. For both the dyes, the absorption intensity was observed to decrease initially and disappear with the increase of irradiation time (at 1 h). This confirms the photocatalytic activity of the prepared films in the UV light region. Figure 9a, b shows the temporal degradation profiles of the CR and MG dyes on exposure to UV light. After testing for 1 h, the degradation efficiencies of the CuO/SnO_2 nanocomposite were found to be 97 and 90% for the CR and MG dyes respectively. The photocatalytic efficiency of the composite is much higher than that of pure CuO and SnO_2 (see Table 2). The enhanced photocatalytic activity of CuO/SnO_2 nanocomposite is due to its synergistic action on the specific adsorption property and efficient electron hole separation at the CuO–SnO_2 photocatalyst boundary.

Kinetic studies

Investigation has been done on the kinetics of the dye degradation. Figure 9c, d shows that the decolonization reaction of the dyes obeys the pseudo-first-order kinetic model [26]. A plot of $\ln(C_0/C_t)$ vs. t was drawn to determine the apparent reaction rate constant (k_{ap}) as a function of the initial dye concentration. The results obtained show that the catalytic activity of the composite CuO–SnO_2 exhibits a faster kinetic rate when compared to the pure CuO and SnO_2.

Recycle test

A cycling experiment was carried out to study the photodegradation of CR and MG dyes under the influence of the catalysts and the corresponding degradation profiles are shown in Fig. 10a, b respectively. No significant decrease of the photocatalytic activity of the nanocomposite was observed

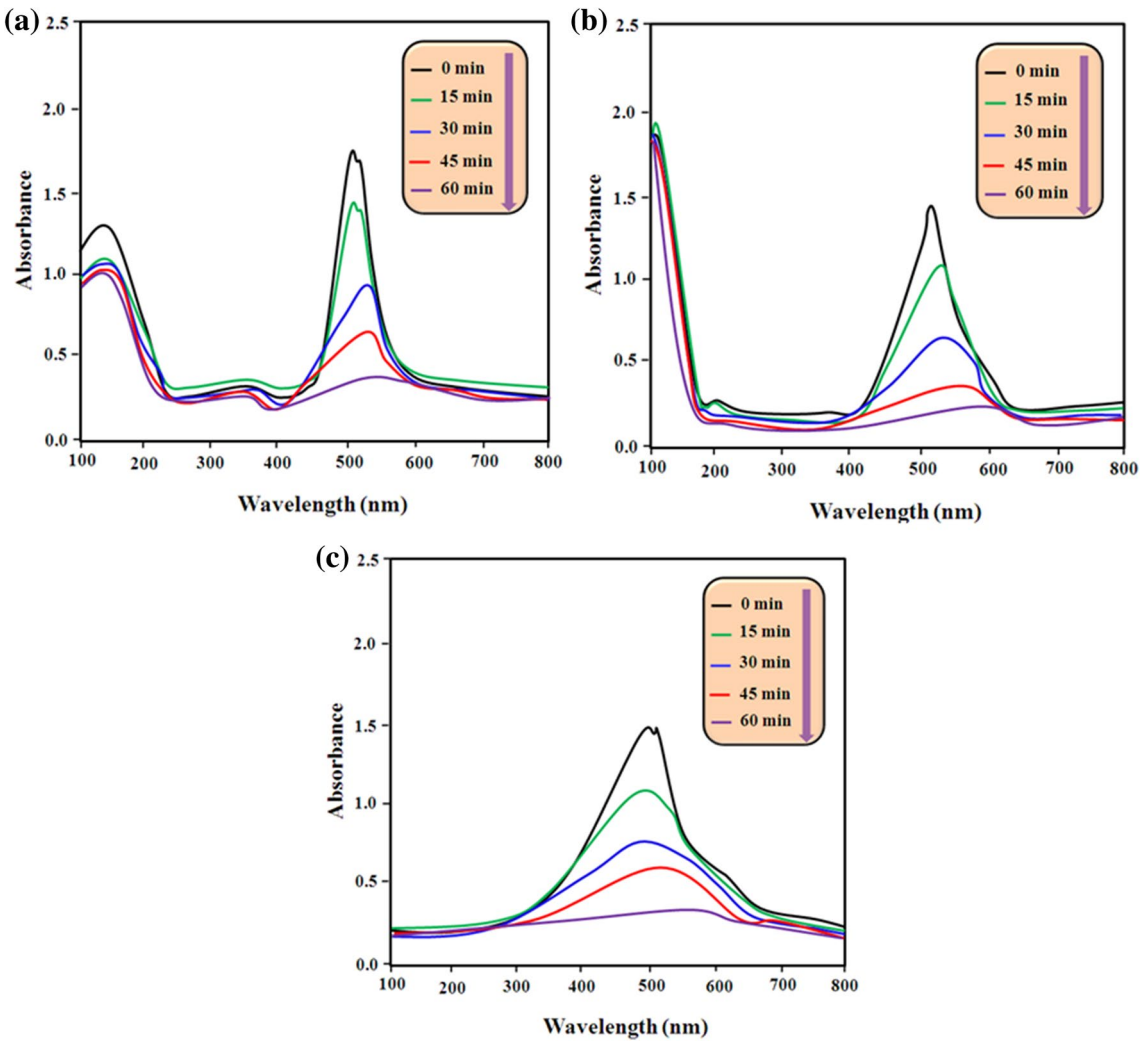

Fig. 7 UV absorption spectra of CR ($\lambda_{max} = 500$ nm) under UV light **a** CuO, **b** SnO_2 and **c** 1:1

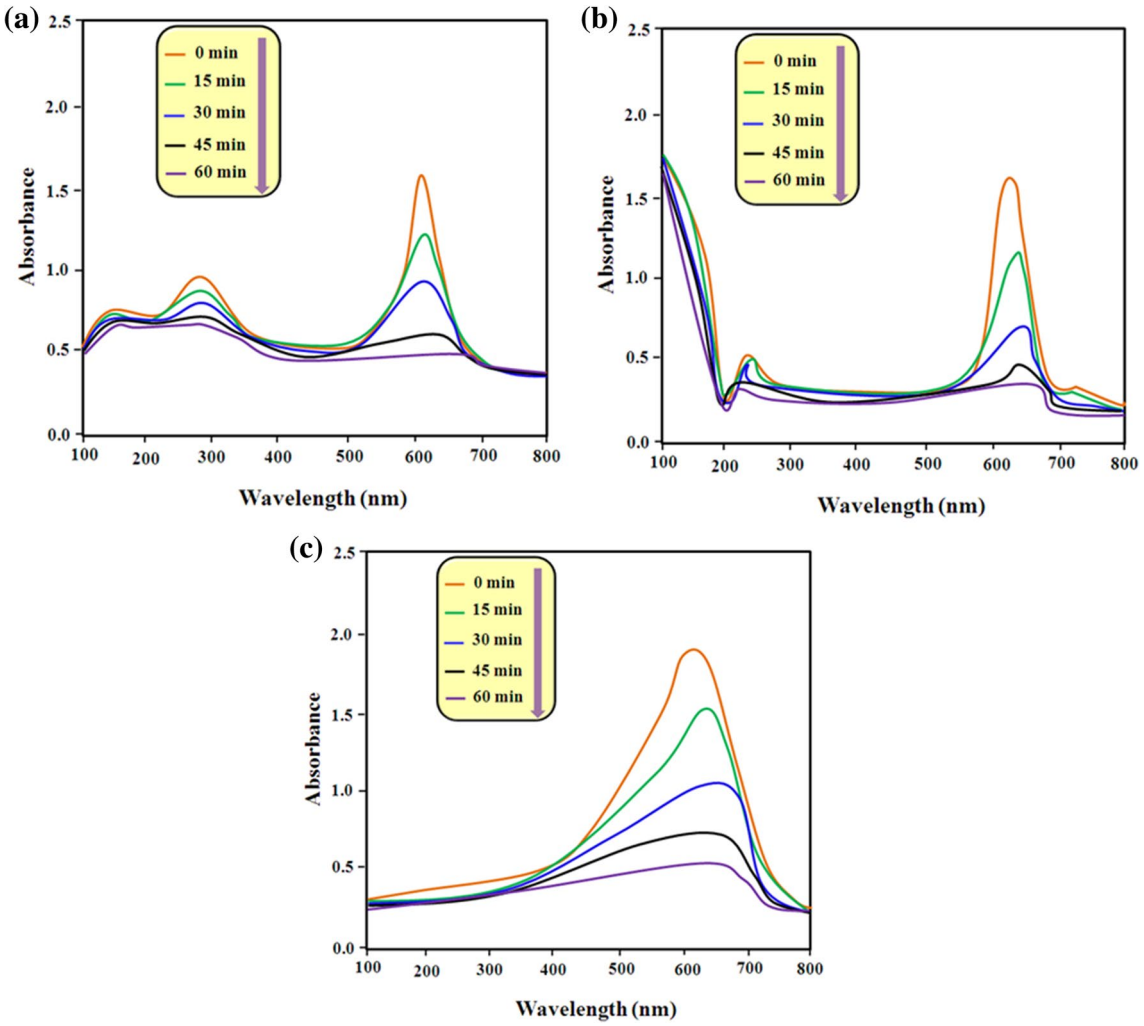

Fig. 8 UV absorption spectra of MG (λ_{max} = 610 nm) under visible light **a** CuO, **b** SnO_2 and **c** 1:1

even after seven cycles (only loss 3–5%). The slight variation observed in the photocatalytic degradation may be attributed to the incomplete collection of the samples during centrifugation. The obtained results suggest that the CuO/SnO_2 nanocomposite has a high potential for use as an efficient and reusable photocatalyst.

Photocatalytic mechanism

The schematic illustration for the possible photocatalytic mechanism of the CuO/SnO_2 nanocomposite on the dyes is shown in Fig. 10c. The CuO/SnO_2 heterojunction, on excitation, can produce photo-generated electrons (e^-) and holes (h^+) in the presence of UV light. The photo-generated electrons produced in the conduction band of CuO jump to the conduction band of SnO_2, and the holes from the valence band of SnO_2 move to the valence band of CuO [27]. The photo-generated electrons react with the adsorbed oxygen to produce active $^{\cdot}O_2^-$ radicals. In addition, the hydroxyl ions (OH^-) are oxidized into hydroxyl radicals (^-OH) by the photo-induced holes. The dye molecules which are decomposed into simple organic molecules by the continuously produced reactive oxidation species are finally transformed into CO_2 and H_2O. The efficient separation of electron–hole pairs in the CuO/SnO_2 nanocomposite is the reason for its superior stability and improved photocatalytic activity on CR and MG dyes under UV light. Moreover, CuO is a p-type narrow band semiconductor with work function of 1.2–1.8 eV, while SnO_2 is n-type wide band semiconductor with work function of 4.52 eV. In the presence of UV light, only CuO is excited because of inter band transitions. SnO_2 remains largely inactive due to its wide band gap. On formation of the CuO–SnO_2 heterojunction, the band gap is reduced to 2.75 eV. It can hence be concluded that the high visible light absorbance of CuO–SnO_2 is responsible for the

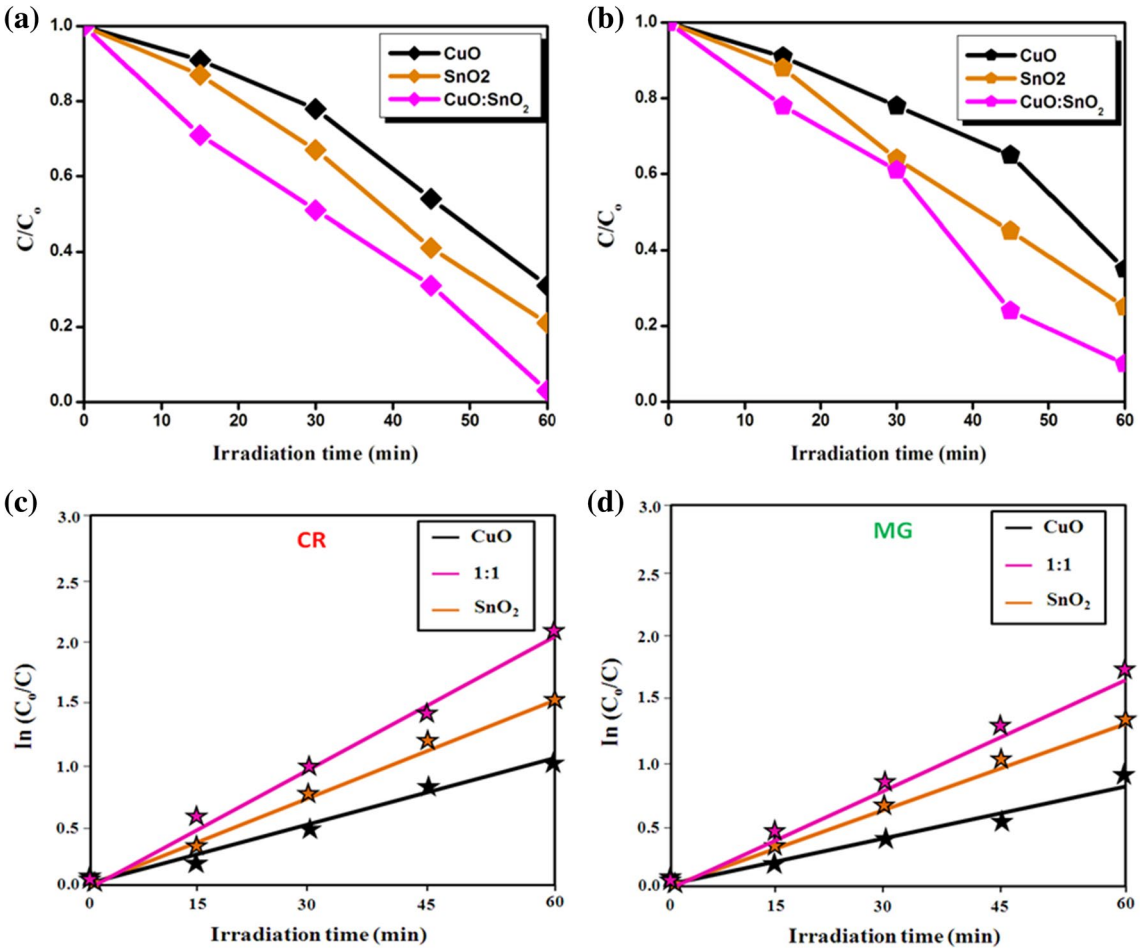

Fig. 9 Temporal degradation profile of **a** CR **b** MG under UV light irradiation; kinetic degradation profile of **c** CR **d** MG under UV light irradiation

Table 2 Shows the photocatalytic parameters of the films

Samples (eV)	Band gap of CR	Rate constant of MG		Rate constant		Degradation efficiency at 60 min	
		K (h^{-1})	R^2	K (h^{-1})	R^2	CR	MG
CuO	1.6	0.121	0.958	0.101	0.971	75	65
SnO_2	3.6	1.157	0.977	1.105	0.968	84	72
1:1	3.0	4.474	0.998	4.401	0.978	97	90

generation of electrons and holes, which in turn improves the photocatalytic activity.

Conclusions

In summary, CuO, SnO_2 and CuO/SnO_2 nanocomposite films were successfully synthesized by spray pyrolysis technique and the structural, optical and photocatalytic properties systematically investigated. The CuO/SnO_2 heterojunctions show excellent photocatalytic degradation efficiency of CR and MG under UV light illumination. The results showed that the CuO–SnO_2 composite exhibits superior photocatalytic performance towards CR such as high degradation efficiency (97%) and long term stability (only loss 3%) after a seven cycles test. The enhanced photocatalytic activity of the CuO/SnO_2 nanocomposite is attributed to the formation of heterojunction and low recombination probability of photo-generated carriers due to the efficient charge transfer between CuO and SnO_2 nanocrystals. Hence,

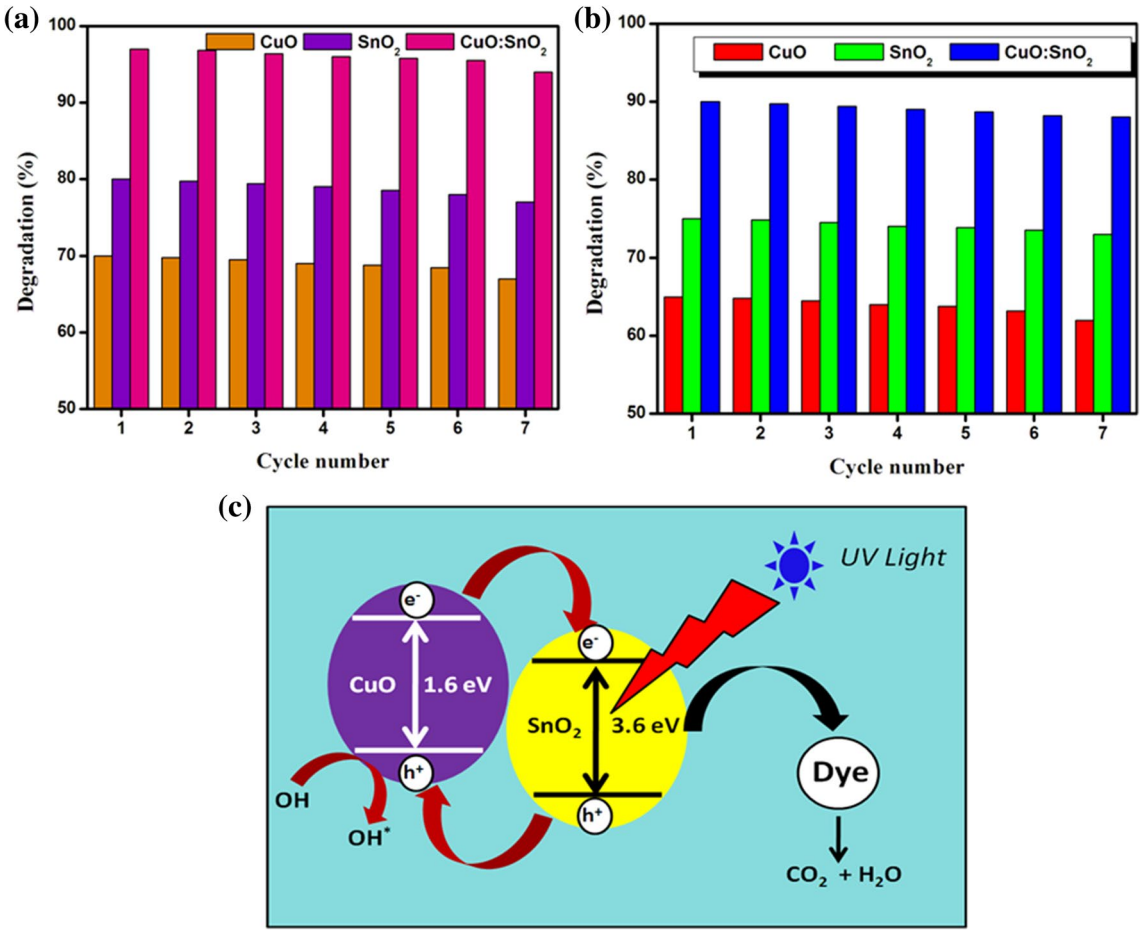

Fig. 10 Seven cycles segment for degradation of **a** CR **b** MG under UV light irradiation **c** schematic representation for photocatalytic mechanism of CuO/SnO_2 composite under UV light

this work may provide new insights into the development of novel UV light photocatalysts for water purification and correlated applications.

References

1. U.I. Gaya, A.H. Abdullah, Z. Zainal, M.Z. Hussein, J. Hazard. Mater. **168**, 57 (2009)
2. S. Mukhopadhyay, P.P. Das, S. Maity, P. Ghosh, P.S. Devi, Appl. Catal. B Environ. **165**, 128 (2015)
3. M.L. Huang, S.X. Weng, B. Wang, J. Hu, X.Z. Fu, P. Liu, J. Phys. Chem. C **118**, 25434 (2014)
4. S. Girish Kumar, K.S.R. Koteswara Rao, RSC Adv. **5**, 3306 (2015)
5. M.R. Kumar, G. Murugadoss, A.N. Pirogov, R. Thangamuthu, J. Mater. Sci. Mater. Electron. **29**, 13508 (2018)
6. W. Zhao, W.H. Ma, C.C. Chen, J.C. Zhao, Z.G. Shuai, J. Am. Chem. Soc. **126**, 4782 (2004)
7. M. Ghanbari, F. Ansari, M. Salavati-Niasari, Inorg. Chim. Acta. **455**, 88 (2017)
8. G. Murugadoss, R. Thangamuthu, R. Jayavel, M. Rajesh Kumar, J. Lumin. **165**, 30 (2015)
9. O. Amiria, N. Mir, F. Ansarid, M. Salavati-Niasari, Electrochim. Acta **252**, 315 (2017)
10. F. Ansari, P. Nazari, M. Payandeh, F.M. Asl, B. Abdollahi-Nejand, V. Ahmadi, J. Taghiloo, M. Salavati-Niasari, Nanotechnology **29**, 075404 (2018)
11. P. Nazari, F. Ansari, B.A. Nejand, V. Ahmadi, M. Payandeh, M. Salavati-Niasari, J. Phys. Chem. C **121**, 21935 (2017)
12. M. Parthibavarmana, V. Hariharan, C. Sekar, Mater. Sci. Eng. C. **31**, 840 (2011)
13. H.-L. Xia, H.-S. Zhuang, T. Zhang, D.-C. Xiao, J. Environ. Sci. **19**, 1141 (2007)
14. A. Kumar, L. Rout, L. Satish Kumar Achary, A. Mohanty, J.M.P.K. Chand, P. Dash, AIP Conf. Proc. **1724**, 020027 (2016)
15. A.T. Rajamanickam, P. Thirunavukkarasu, K. Dhanakodi, J. Mater. Sci. Mater. Elec. **26**, 8933 (2015)
16. M. Parthibavarman, K. Vallalperuman, S. Sathishkumar, M. Durairaj, K. Thavamani, J. Mater. Sci. Mater. Electron. **25**, 730 (2014)
17. M. Ahmad, E. Ahmed, Y. Zhang, N.R. Khalid, J. Xu, M. Ullah, Z. Hong, Curr. Appl. Phys. **13**, 697 (2013)
18. L.M. Fang, X.T. Zu, Z.J. Li, S. Zhu, C.M. Liu, L.M. Wang, F. Gao, J. Mater. Sci. Mater. Electron. **19**, 868 (2008)
19. V. Kumar, V. Kumar, S. Som, J.H. Neethling, M. Lee, O.M. Ntwaeaborwa, H.C. Swart. Nanotechnology **25**, 135701 (2014)

20. J. Koshy, M. Soosen Samuel, A. Chandran, K.C. George, AIP Conf. Proc. **1391**, 576 (2011)
21. J.H. He, T.H. Wu, C.L. Hsin, K.M. Li, L.J. Chen, Y.L. Chueh, L.J. Chou, Z.L. Wang, Small **2**, 116 (2006)
22. M. Sabarilakshmi, K. Janaki, J. Mater. Sci. Mater. Electron. **28**, 5329 (2017)
23. L. Chen, L. Li, G. Li, J. Alloy. Compd. **464**, 532 (2008)
24. M. Parthibavarman, V. Sharmila, P. Sathishkumar, S.A. Gaikwad, J. Electron. Mater. **47**, 5443 (2018)
25. D. Shaposhnik, R. Pavelko, E. Llobet, F. Gispert-Guirado, X. Vilanova, Int. J. Hydrog. Energy. **34**, 3621 (2009)
26. A. Bokare, A. Sanap, M. Pai, S. Sabharwal, A.A. Athawale, Colloids Surf. B Biointerface **102**, 273 (2013)
27. D. Li, J. Hu, R. Wu, J.G. Lu, Nanotechnology **21**, 485502 (2010)